

pubs.acs.org/acssensors Article

# Constant Conversion Rate of Endolysosomes Revealed by a pH-Sensitive Fluorescent Probe

Rui Chen, Lei Wang, Guodong Ding, Guanqun Han, Kangqiang Qiu, Yujie Sun,\* and Jiajie Diao\*



Cite This: ACS Sens. 2023, 8, 2068-2078



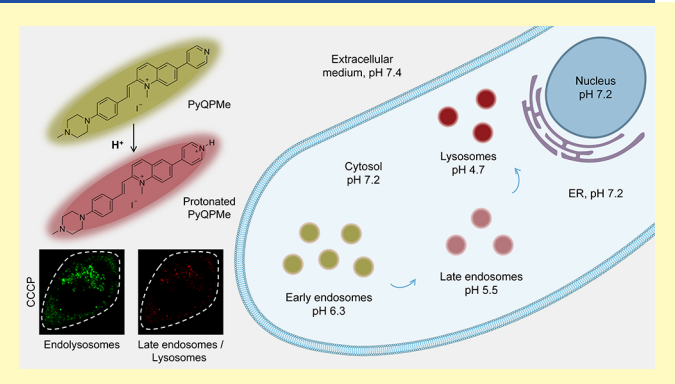
**ACCESS** 

Metrics & More

Article Recommendations

Supporting Information

ABSTRACT: Endolysosome dynamics plays an important role in autophagosome biogenesis. Hence, imaging the subcellular dynamics of endolysosomes using high-resolution fluorescent imaging techniques would deepen our understanding of autophagy and benefit the development of pharmaceuticals against endosome-related diseases. Taking advantage of the intramolecular charge-transfer mechanism, herein we report a cationic quinolinium-based fluorescent probe (PyQPMe) that exhibits excellent pH-sensitive fluorescence in endolysosomes at different stages of interest. A systematic photophysical and computational study on PyQPMe was carried out to rationalize its highly pH-dependent absorption and emission spectra. The large Stokes shift and strong fluorescence intensity of PyQPMe can effectively reduce the



background noise caused by excitation light and microenvironments and provide a high signal-to-noise ratio for high-resolution imaging of endolysosomes. By applying PyQPMe as a small molecular probe in live cells, we were able to reveal a constant conversion rate from early endosomes to late endosomes/lysosomes during autophagy at the submicron level.

KEYWORDS: endolysosome dynamics, high-resolution imaging, fluorescent probe, pH sensitivity, quantitative biology

utophagy is a conserved lysosomal degradation pathway, Awhich maintains cellular homeostasis and health by removing unnecessary or dysfunctional substances. 1-3 Endolysosomes, including early endosomes, late endosomes, and lysosomes, are critical for autophagosome biogenesis during the process of autophagy<sup>4,5</sup> and hence imaging the subcellular dynamics of endolysosomes with a high spatial-temporal resolution will significantly benefit our understanding of autophagy and will also provide the opportunity to develop new therapeutic strategies for lysosome-related neurological disorders, such as Alzheimer's disease.<sup>6,7</sup> Our previous research has shown that the number of lysosomes increases dramatically during autophagy, while the mechanism behind it remains unknown.8 This raises an important biological question: what is the reason behind the dramatic increase in lysosomes during autophagy? Does the augmentation of the total endolysosome number or the accelerated conversion rate from early to late endosomes/lysosomes contribute to the increasing number of lysosomes during autophagy? Therefore, it is vital to develop an appropriate probe to study the endolysosome dynamics by illustrating the different stages of endolysosomes with different fluorescence signals.

Designing high-performance fluorescent probes suitable for in situ real-time bioimaging faces a set of challenges. Strict criteria are required, including specific targeting ability, high sensitivity, long-term photostability, high signal-to-noise ratio, and low toxicity. In the past few years, scientists have developed a series

of cell-permeable organic fluorophores for lysosomes with various colors that exhibit great bioimaging properties.<sup>9,10</sup> To further observe the dynamics of lysosomes, the general microenvironment changes in lysosomes can be used as versatile and effective markers, such as viscosity and polarity. 11-16 Since the local pH decreases substantially from early endosome (pH 6.3) to late endosome (pH 5.5) and lysosome (pH  $\sim$  4.7) while the extracellular medium, cytosol, and nucleus all maintain a nearly neutral pH 7.2-7.4, such a significant pH difference of endolysosomes at different stages can be utilized in designing fluorescent probes for tracking their dynamics. 18-24 Recently, real-time imaging of the cellular uptake via endocytosis has been successfully achieved by using a pH-sensitive lysosomal fluorophore. in which protonation occurs on a neutral phenol moiety.<sup>25</sup> However, most reported pH-sensitive probe designs only result in "turn-on" probes at low pH, which are nearly non-fluorescent at high pH, or vice versa. 26,27 In order to precisely track the dynamics of endolysosomes via fluorescence microscopy techniques, it is necessary to design novel probes

Received: February 21, 2023 Accepted: April 24, 2023 Published: May 4, 2023





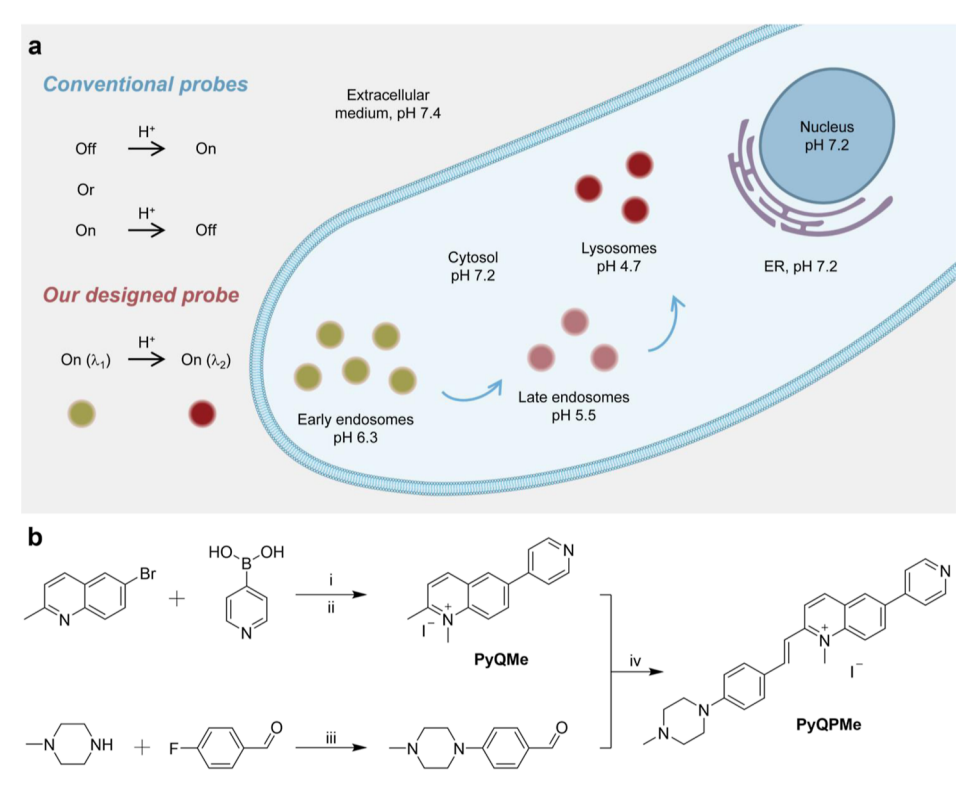


**Figure 1.** Schematic of design and synthesis of PyQPMe. (a) Proposed design of a pH-dependent probe to track the endolysosome dynamics. (b) Synthetic scheme of the designed fluorescent probe PyQPMe. (i) Pd(PPh<sub>3</sub>)<sub>4</sub>, K<sub>2</sub>CO<sub>3</sub>, (Bu)<sub>4</sub>NBr, toluene, EtOH, H<sub>2</sub>O, N<sub>2</sub>, 100 °C; (ii) CH<sub>3</sub>I, EtOH or CH<sub>3</sub>CN, 80 °C; (iii) K<sub>2</sub>CO<sub>3</sub>, DMF, 100 °C; and (iv) anhydrous EtOH, N<sub>2</sub>, 80 °C.

with pH-dependent evolution and large Stokes shifts that can be imaged simultaneously in multiple channels with low background noise.

On the other hand, even though fluorescence microscopy has demonstrated its value in the visual analysis of substances within cells as well as living organisms, the practical resolution limit of optical microscopes (roughly 200 nm) restricts its applicability.<sup>28</sup> Recently, several novel high-resolution microscopes that can break diffraction limits have been invented for cell imaging to digitize and observe the dynamic changes and interactions of organelles.<sup>29-33</sup> LIGHTNING is a Leica ultrahigh-resolution confocal platform, which is based on adaptive computational deconvolution and has overcome the resolution down to 120 nm with simultaneous multicolor imaging. 34,35 With the LIGHTING mode, the details of living samples can be efficiently tracked with fast acquisition speed, and it can greatly prevent photodamage caused by using high-energy laser sources.<sup>36,37</sup> Nevertheless, the design of high-resolution fluorescent probes remains limited in terms of background noise, photobleaching, and wavelength selection.

In this study, we designed a cationic quinolinium-based fluorescent probe, named as PyQPMe. This small-molecule probe PyQPMe allows one to simultaneously monitor two fluorescence signals in endolysosomes at different stages of interest and minimizes the interference from various microenvironments; and its large Stokes shift and strong fluorescence intensity properties endow a high signal-to-noise ratio for high-resolution imaging (Figure 1a). By utilizing this probe for imaging, the dynamics of endolysosomes was further digitized and characterized, which revealed a constant conversion rate from early endosomes to late endosomes/lysosomes during autophagy.

#### RESULTS AND DISCUSSION

Design and Synthesis of PyQPMe. Inspired by the rich photophysical properties resulting from intramolecular charge transfer in organic fluorophores, we sought to develop a novel fluorescent probe composed of both electron-donating (e.g., piperazine) and electron-withdrawing (e.g., cationic quinolinium moiety) units connected by a C=C double bond. Piperazine is selected as an ideal electron-donating group because it is also a good targeting group toward endolysosomes.<sup>38</sup> Furthermore, intending to introduce pH-dependent optical responses for tracking the endolysosome dynamics, we reasoned that installing a pyridyl substituent would be an attractive option because the p $K_a$  of pyridine is 5.23, <sup>39</sup> perfectly falling within the pH range from early endosomes to lysosomes. 40 Hence, we report a fluorescent probe with pH sensitivity toward endolysosomes, which can be employed as a convenient tool to investigate the endolysosome dynamics in real time by using high-resolution imaging techniques with high spatial resolution and low background noise.

The synthetic scheme of PyQPMe is presented in Figure 1b, wherein the initial step is the Suzuki coupling between 6-bromo-2-methylquinoline and pyridine-4-ylboronic acid, both of which are commercially available. Subsequent methylation at the quinoline N resulted in the intermediate product PyQMe with an overall yield above 50%. On the other hand, reaction between 1-methylpiperazine and *p*-fluorobenzaldehyde under alkaline condition led to the formation of 4-(4-methylpiperazin-1-yl) benzaldehyde in a nearly quantitative yield. A final Knoevenagel condensation between PyQMe and 4-(4-methylpiperazin-1-yl) benzaldehyde realized the synthesis of PyQPMe. The experimental details and characterization for the syntheses of

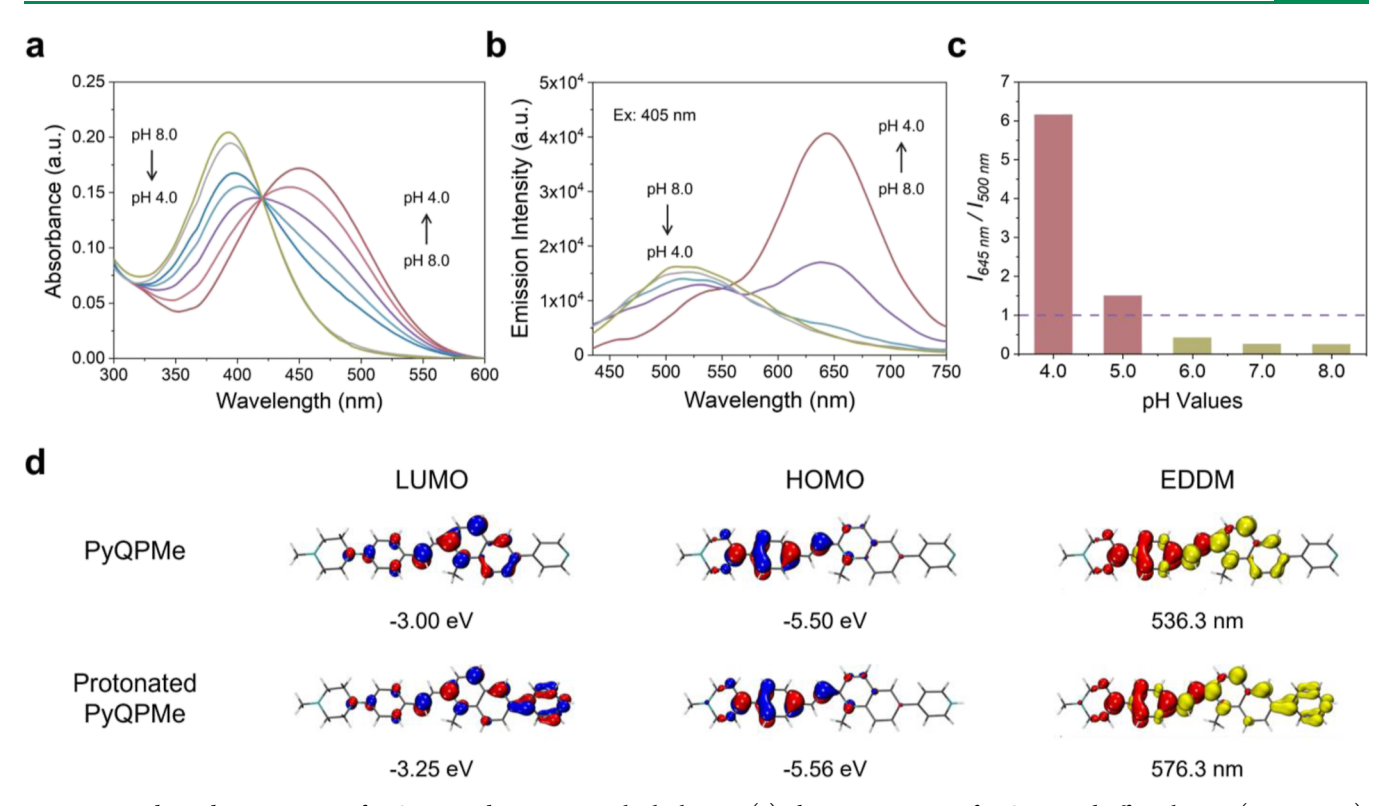


Figure 2. pH-dependent properties of PyQPMe and computational calculations. (a) Absorption spectra of PyQPMe in buffer solutions (pH 4.0–8.0). (b) Emission spectra of PyQPMe in buffer solutions with different pH values excited at 405 nm. (c)  $I_{645\text{nm}}/I_{500\text{nm}}$  emission intensity ratio of PyQPMe in buffer solutions (pH 4.0–8.0). (d) Calculated HOMOs, LUMOs, and EDDMs of the first singlet excited states ( $S_1$ ) of PyQPMe and protonated PyQPMe. Red and yellow indicate decrease and increase in electron density, respectively. Isovalue = 0.04 for plotting HOMOs, LUMOs, and EDDMs.

PyQPMe and relevant synthetic intermediates are included in the Supporting Information (Figures S1—S5).

pH-Dependent Properties of PyQPMe and Computational Calculations. With the designed probe PyQPMe in hand, we screened its UV-visible absorption in aqueous buffers with a pH range of 8.0-4.0. To our delight, PyQPMe exhibited substantial spectral evolution along with the pH change, as presented in Figure 2a. Under the neutral condition, PyQPMe has an absorption maximum at 394 nm ( $\varepsilon = 34,147 \text{ M}^{-1} \text{ cm}^{-1}$ , Figure S6 and Table S1), which readily decreases when the pH is below 6. Simultaneously, a new absorption maximum at 447 nm ( $\varepsilon$  = 27,264 M $^{-1}$  cm $^{-1}$ ) rises with its tail exceeding 600 nm in pH 4.0 buffer solution. The absorption intensity evolution at 394 and 447 nm along with the decrease of pH from 8.0 to 4.0 faultlessly elaborate an apparent p $K_a$  value of ~5 for PyQPMe. In the meantime, PyQPMe remains fluorescent within the entire pH window of 8.0 to 4.0. Under 405 nm excitation, PyQPMe showed fluorescence with a maximum peak at 510 nm in the neutral solution (Figure 2b). When the pH decreased from 8.0 to 4.0, the PyQPMe probe displayed a 140 nm red-shift with a new emission peak at 650 nm. The Stokes shift of PyQPMe in acid solution is greater than 200 nm, which is due to the extended  $\pi$ -conjugation and enhanced intramolecular charge transfer induced by the protonation of its terminal pyridine group. The quantum yield of PyQPMe was also enhanced to 0.23% in pH 4.0 buffer solution (Table S2). Moreover, the pH titration curve illustrated a decent linear relationship by plotting the emission intensity ratio of  $I_{510\text{nm}}/I_{650\text{nm}}$  against pH values (Figure S7). In addition, the fluorescence intensities of PyQPMe used for different imaging channels of the microscope were compared, where the wavelengths of 500 and 645 nm represent the green and red channels, respectively. When the buffer

solution is much more acidic, the fluorescence intensity ratio of  $I_{645\text{nm}}/I_{500\text{nm}}$  is higher than 1 (Figure 2c), indicating that red color dominates the fluorescence of PyQPMe. Conversely, with increasing the pH value, green fluorescence light is becoming the predominant color for imaging. This exceptional color evolution property of PyQPMe indicates that it is an ideal pH-sensitive probe for high-resolution imaging in a dual-channel mode.

Next, we investigated the effect of potential biochemical species on the fluorescence intensity of PyQPMe in both pH 3.0 and 8.2 buffer solutions. As shown in Figure S8, various chemical substances, such as cations (K<sup>+</sup>, Na<sup>+</sup>, Mg<sup>2+</sup>, Zn<sup>2+</sup>, Fe<sup>2+</sup>, Fe<sup>3+</sup>, Ag<sup>+</sup>, and  $Ni^{2+}$ ), anions (F<sup>-</sup>, Cl<sup>-</sup>, Br<sup>-</sup>, I<sup>-</sup>, SCN<sup>-</sup>, NO<sub>3</sub><sup>-</sup>, HCO<sub>3</sub><sup>-</sup>, SO<sub>4</sub><sup>2-</sup>, HSO<sub>3</sub><sup>-</sup>, and Ac<sup>-</sup>), reactive oxygen species (H<sub>2</sub>O<sub>2</sub>), and reactive sulfur species (Cys, Hcy, and GSH) were added to the PyOPMe solution; none of these interfering substances could quench the emission intensity in either pH 3.0 or 8.2 solutions, and the protonated PyQPMe exhibited strong fluorescence during the whole process. Besides, we obtained the fluorescence spectra of PyQPMe in various solvents with different polarities. As illustrated in Figure S9, PyQPMe only exhibited significant emission intensity in low pH solution, further confirming that polarity has no effect on the fluorescence of PyQPMe. In addition, as a pH probe, the emission spectra of PyQPMe show excellent reversibility between pH 8.5 and pH 3.0 (Figure S10), which is attributed to the protonation/deprotonation of its terminal pyridine group. Furthermore, the photostability of PyQPMe was investigated under different pH conditions. As depicted in Figure S11, the fluorescence intensity exhibited negligible change after 300 s irradiation in neutral and acidic solutions, confirming its superior photostability. Taken together, the above photophysical results strongly suggest that PyQPMe could be a promising pH-sensitive probe, well suited for

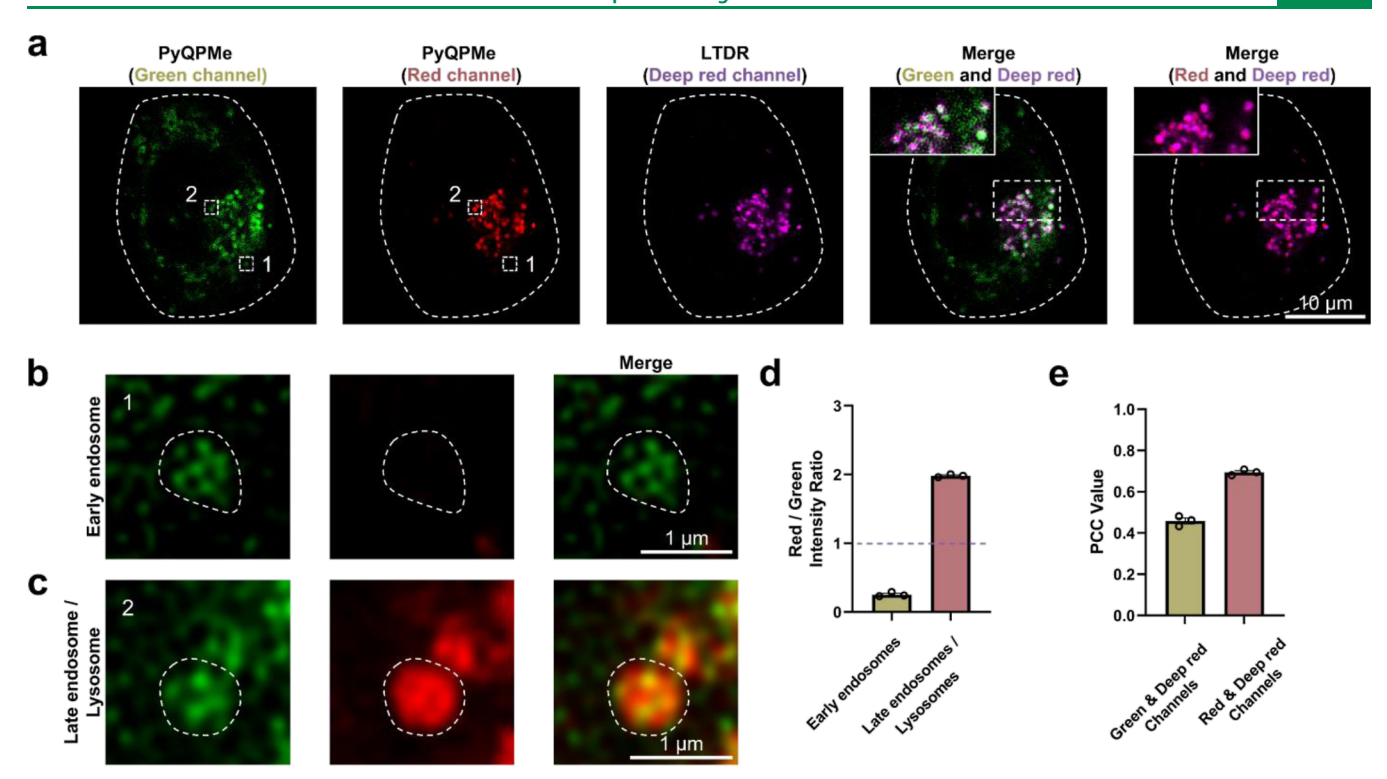


Figure 3. Characterization of PyQPMe in living cells. (a) Confocal imaging of PyQPMe co-stained with LTDR in HeLa cells. (b,c) Zoom-in images of white rectangles in (a). (d) Red to green fluorescence intensity ratio of PyQPMe-stained early endosomes and late endosomes/lysosomes. (e) PCC value of PyQPMe co-stained with LTDR. Green channel,  $\lambda_{\rm ex}$  = 405 nm,  $\lambda_{\rm em}$  = 470–530 nm; red channel,  $\lambda_{\rm ex}$  = 405 nm,  $\lambda_{\rm em}$  = 610–680 nm; and deep red channel,  $\lambda_{\rm ex}$  = 640 nm,  $\lambda_{\rm em}$  = 690–740 nm.

studying endolysosome dynamics via high-resolution imaging techniques.

To shed light on the pH-dependent photophysical properties of PyQPMe, we further performed density functional theory (DFT) calculations on PyQPMe (Tables S3 and S4) and protonated PyQPMe (protonation at the pyridine unit, Tables S5 and S6). As shown in Figure 2d, the highest occupied molecular orbitals (HOMOs) of both compounds are located at their electron-donating phenyl piperazine side, as expected. The lowest unoccupied molecular orbital (LUMO) of PyQPMe is primarily centered on the methylated quinolinium moiety. In sharp contrast, the LUMO of the protonated PyQPMe has a much wider electron density distribution toward the terminal protonated pyridine, in agreement with its increased positive charge after protonation. Therefore, even though their HOMOs have similar energies (-5.50 and -5.56 eV), the LUMO of the protonated PyQPMe (-3.25 eV) is 0.25 eV lower in energy than that of PyQPMe (-3.00 eV). With such a significant deviation in energy and distribution of the LUMOs from PyQPMe to the protonated PyQPMe, it is well anticipated that the lowest singlet excited state (S<sub>1</sub>, primarily from HOMO to LUMO transition) of PyQPMe will show a red-shift accordingly after protonation. Indeed, the S<sub>1</sub> states of PyQPMe before and after protonation were computed to be located at 536.3 and 576.3 nm, respectively (Figure S12). Furthermore, the calculated electron density difference maps (EDDMs) of their S<sub>1</sub> states vividly elaborate the change of electron density, where yellow and red imply increase and decrease in electron density, respectively (Figure 2d).

Characterization of PyQPMe in Living Cells. To take advantage of the absorption and emission spectra of PyQPMe, we applied this probe in high-resolution microscopy for living cells. The toxicity of PyQPMe was examined at first before

characterizing its imaging properties. Cell counting kit-8 (CCK-8) was used to investigate the viability of HeLa cells stained with PyQPMe. As shown in Figure S13, PyQPMe exhibited no effects on the viability of HeLa cells within 24 h incubation at concentrations of  $0-10 \mu M$ . The probe's high hydrophilicity [n-10]octanol/water partition coefficient (log *P*)  $\sim$  -0.65, Figure S14] indicates that it enters the cell through endocytosis instead of penetrating freely through cell membranes. 41-43 Next, PyQPMe was characterized by a Leica Stellaris Confocal Microscope in the LIGHTNING module for high-resolution imaging. Under an excitation of 405 nm imaging channel and an incubation time of 10 min, we found that PyQPMe entered HeLa cells and showed punctate fluorescence signals in the cytoplasm (Figure S15). The signal tended to be endolysosomes because endolysosomes have a low pH range from 4.7 to 6.3. When treating HeLa cells with a high concentration (2  $\mu$ M) of PyQPMe, the same fluorescence signal inside HeLa cells could be observed, suggesting the intake of PyQPMe is through endocytosis. Additionally, it was noted that a significant reduction in fluorescence occurred following treatment with the endocytic inhibitors, 44-46 chloroquine, and NH<sub>4</sub>Cl (Figure \$16), implying that the process of endocytosis is accountable for the uptake of PyQPMe. Since low temperatures can inhibit endocytosis, we performed experiments at a lower temperature. 47 Fewer endolysosomes were detected in cells incubated at a temperature of 4 °C than 37 °C (Figure S17), further confirming that the uptake of PyQPMe is an ATP-dependent endocytosis pathway. In addition, PyQPMe can also be used in other cell lines, such as the rat-derived PC12 cells containing more endolysosomes than human-derived HeLa cells (Figure S18).

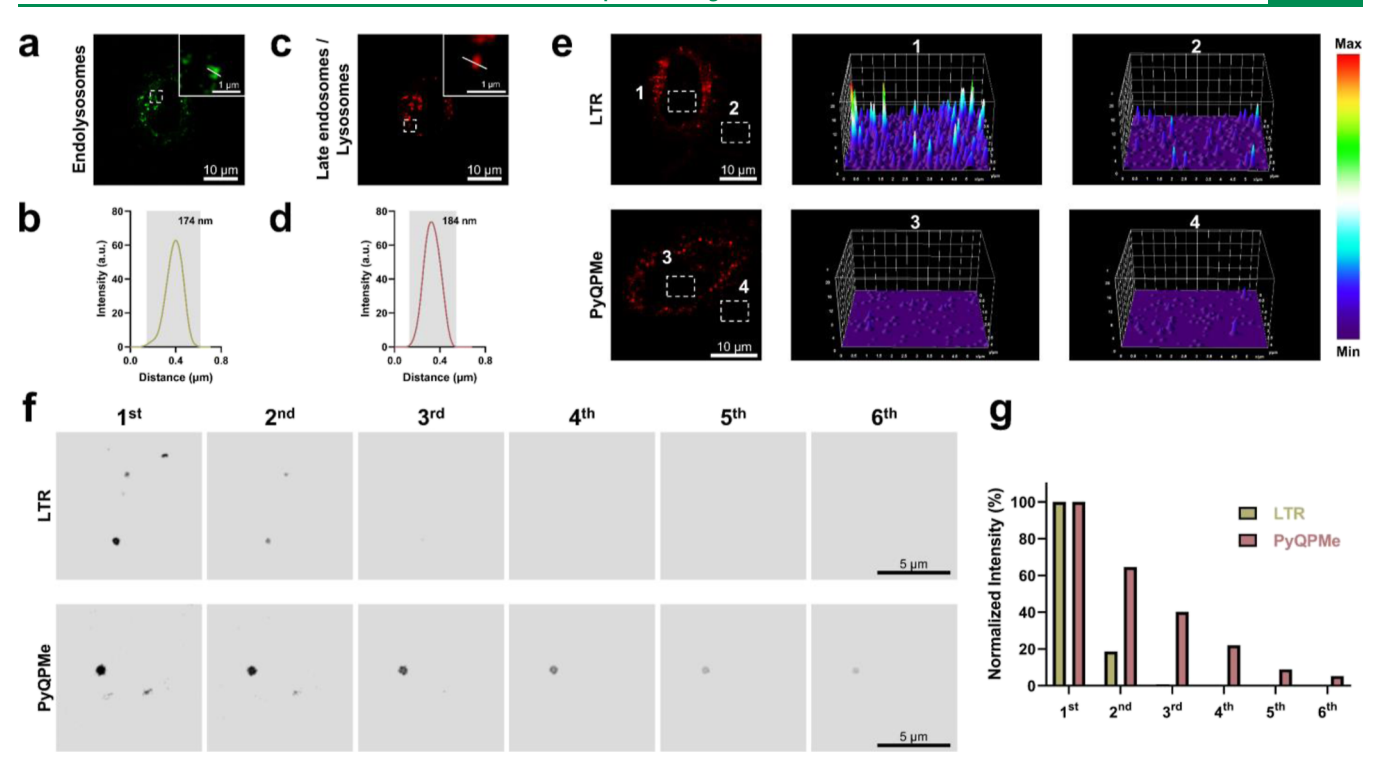


Figure 4. Characterization of imaging properties of PyQPMe-stained endolysosomes. (a) Confocal image of PyQPMe-stained endolysosomes and fluorescence intensity profile (b) of the write line in (a). (c) Confocal image of PyQPMe-stained late endosomes/lysosomes and fluorescence intensity profile (d) of the write line in (c). (e) Confocal images of HeLa cells labeled with LTR and PyQPMe and 3D fluorescence intensity plots of rectangles of integration. (f) Continuous imaging of HeLa cells labeled with LTR or PyQPMe at 100% laser intensity for photobleaching, and each scan time was 10 s, images were captured under a red channel. (g) Normalized fluorescence intensity of LTR and PyQPMe in (f).

Next, imaging studies of PyQPMe were performed under a dual channel mode with the same excitation of 405 nm (green channel, emission range of 470-530 nm; red channel, emission range of 610-680 nm). Due to the strong green emission properties of PyQPMe over a wide pH range, many puncta fluorescence appeared throughout the cell in the green channel image (Figure 3a). While in the red channel image, there is less puncta fluorescence in the cell because PyQPMe only emits red light at pH values below 6. Therefore, this imaging property of PyQPMe at different channels can guide us to track different stages of endocytosis. We then randomly zoomed-in images and compared their fluorescence intensity. As shown in Figure 3b,d, early endosomes exhibited clear green fluorescence with a very low ratio of red to green fluorescence intensity. In contrast, due to the low pH value in late endosomes/lysosomes, PyQPMe displayed both green and red fluorescence, and the ratio of red to green intensity was higher than 1 (Figure 3c,d), in full agreement with our previous photophysical expectations. Besides, the average diameter of PyQPMe red spots is around 0.6  $\mu$ m (Figure S19), which is in line with the reported size of lysosomes. <sup>29,32</sup> To further verify the targeting ability of PyQPMe, we co-stained the cell with commercial lysosome dye Lyso-Tracker Deep Red (LTDR) and imaged it under a deep red channel (excitation of 640 nm and emission range of 690-740 nm). The results showed that the red channel puncta of PyQPMe overlaid well with the deep red channel puncta of LTDR, and the Pearson correlation coefficient (PCC) value was about 0.70 (Figure 3a,e). While the green channel particles of PyQPMe showed less overlap with the deep red channel of LTDR, the PCC value was 0.46, confirming the presence of early endosomes with a higher pH than lysosomes in the green channel images of PyQPMe.

All the above imaging results demonstrate that the terminal pyridine group of PyQPMe is gradually protonated in the cell through the occurrence of endocytosis, resulting in a red-shift of fluorescence. Therefore, due to the different pH values of endolysosomes at different stages, PyQPMe stains total endolysosomes and late endosomes/lysosomes with green and red fluorescence, respectively.

Characterization of Imaging Properties of PyQPMe-Stained Endolysosomes. Based on the above outstanding photophysical properties, PyQPMe is expected to have superior imaging performance. We first compared the fluorescence images of PyQPMe before and after the LIGHTNING module. The confocal images deconvolved by the LIGHTNING module showed better imaging quality, greater precision, higher resolution, and less background fluorescence than those of raw confocal images (Figure S20). To test the resolution limit of PyQPMe, we stochastically selected confocal images and underlined the areas with luminescence in the images (Figure 4a,c). The full width at half-maximum of these bright puncta fluorescence of PyQPMe-stained endolysosomes and later endosomes/lysosomes are down to 174 and 184 nm (Figure 4b,d), respectively.

Since PyQPMe has a large Stokes shift and strong fluorescence intensity, it can effectively reduce the background noise caused by excitation light and microenvironments. To illustrate this merit, we selected a commercial lysosome dye (LysoTracker Red, LTR) for comparison. We randomly chose two different regions of the background in each fluorescence image and plotted their 3D fluorescence intensity distribution maps, as shown in Figure 4e. The results showed that under the same imaging conditions, the background fluorescence of the confocal images of PyQPMe was significantly reduced, and the

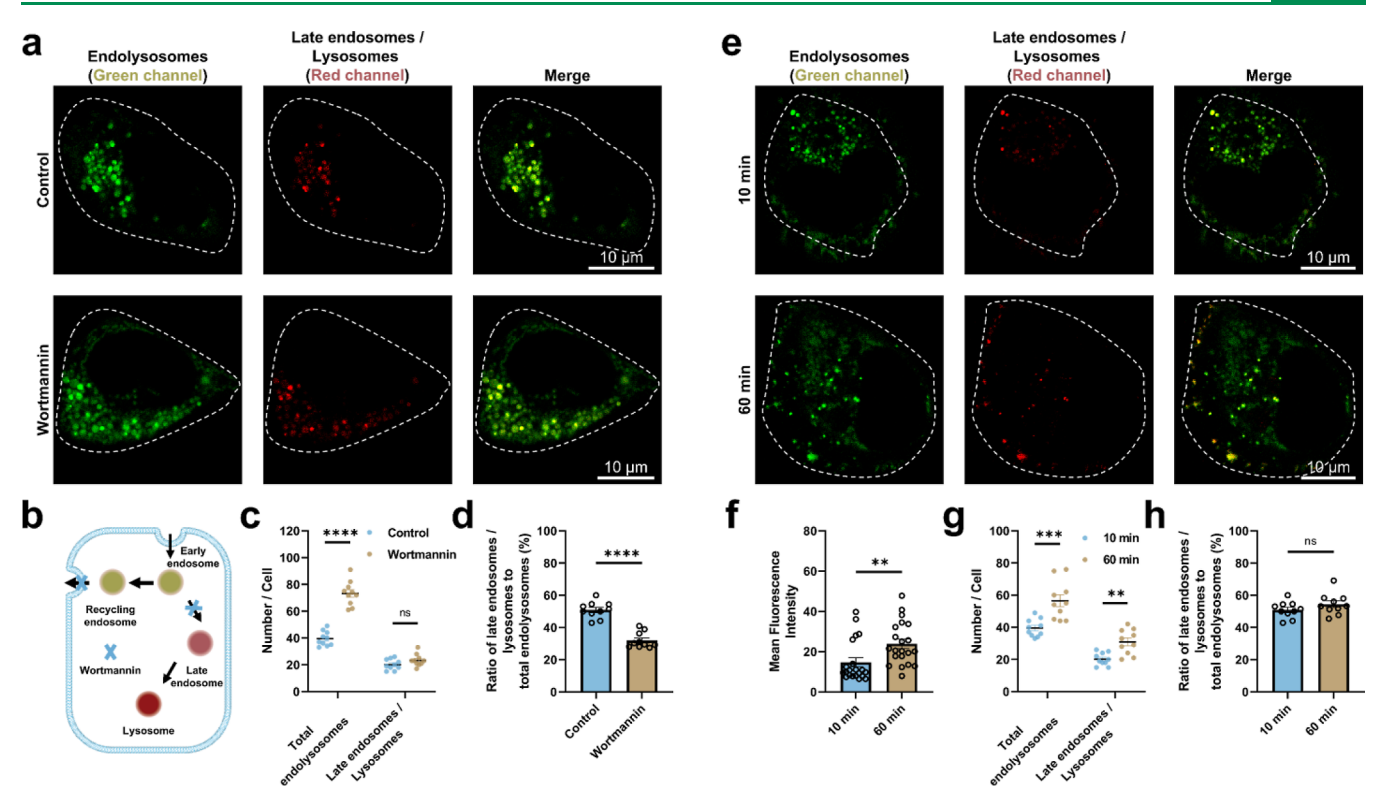


Figure 5. Characterization of dynamics of PyQPMe-stained endolysosomes. (a) Confocal images of HeLa cells stained with PyQPMe following treatment with or without wortmannin for 24 h. (b) Schematic illustration of the effect of wortmannin which inhibits the conversion from early endosomes into late endosomes. (c) Quantification of total endolysosomes and late endosomes/lysosomes in PyQPMe-stained HeLa cells with or without wortmannin treatment. (d) Ratio of the number of late endosomes/lysosomes to total endolysosomes in PyQPMe-stained HeLa cells treated with or without wortmannin. (e) Confocal images of HeLa cells stained with PyQPMe for 10 and 60 min. (f) Mean red puncta fluorescence intensity of PyQPMe-stained HeLa cells for 10 and 60 min incubation. (g) Quantification of total endolysosomes and late endosomes/lysosomes in PyQPMe-stained HeLa cells for 10 and 60 min. (h) Ratio of the number of late endosomes/lysosomes to total endolysosomes in PyQPMe-stained HeLa cells for 10 and 60 min. Data are given as  $M \pm \text{SEM}$  (n = 10 independent samples from 10 cells for each statistical analysis); the statistical differences were analyzed by Student's t test, p < 0.05 is considered to be statistical significant (\*\* $p \le 0.01$ ; \*\*\* $p \le 0.001$ ; \*\*\*\* $p \le 0.001$ ; in p > 0.05).

signal-to-noise ratio was better than that of LTR. Hence, the low background noise is an advantage of PyQPMe for studying the hyperfine structures of cells.

Resistance to photobleaching is a crucial property of probes that determines whether they can be used for long-term fluorescence tracking. To characterize this property, we performed a photobleaching comparison experiment between LTR and PyQPMe in HeLa cells (Figures 4f and S21). When we exposed them to continuous confocal laser at 100% power, the fluorescence intensity of LTR disappeared rapidly after two scans, while the fluorescence signal of PyQPMe maintained 22% of its original value after 40 s of scans (Figure 4g), thereby indicating that PyQPMe has better resistance to photobleaching than the commercial dye. Taken together, these excellent imaging properties of PyQPMe imply that it is a promising probe for high-resolution imaging.

Characterization of the Dynamics of PyQPMe-Stained Endolysosomes. Because of the popularity of quantitative cell biology, it is very crucial to design powerful tools that can digitize individual cells and subcellular organelles to elucidate biological problems in detail. With its great pH response, long-term photostability, and excellent signal-to-noise ratio for high-resolution imaging, PyQPMe was successfully used to track the dynamics of endolysosomes within cells by counting the number of puncta fluorescence signals in both green and red channels (Figures 5a and S22). First, we used wortmannin, a protein inhibitor of phosphoinositide 3-kinases, to inhibit early

endosomes from maturating into late endosomes (Figure 5b). 48-50 After blocking endocytosis by wortmannin treatment for 24 h, the number of endolysosomes was much higher than that in untreated cells (Figures 5a,c and \$23). Besides, the percentage of late endosomes/lysosomes in total endolysosomes was significantly decreased in cells pretreated with wortmannin (Figure 5d), further confirming that wortmannin inhibits maturation from early endosomes into late endosomes and recycles more endosomes within the cells.

Next, we tested the effects of different incubation times on the endocytic pathway. HeLa cells were imaged in green and red channels after 10 and 60 min incubation with PyQPMe, as shown in Figure 5e. First, with the conversion from early endosomes to late endosomes/lysosomes, the intensity of puncta fluorescence in the red channel increased during 60 min incubation (Figure 5f), hence proving that this high intensity of dots is due to the low pH of late endosomes and lysosomes. Second, more PyQPMe-stained total endolysosomes and late endosomes/lysosomes were simultaneously detected in HeLa cells incubated for 60 min when compared to the number of endolysosomes in PyQPMe-stained cells incubated for 10 min (Figures 5g and S24), as expected. Surprisingly, the percentage of late endosomes/lysosomes in total endolysosomes remained stable regardless of incubation time, as exhibited in Figure 5h. These results indicate that PyQPMe can be effectively used to digitize and track endocytosis to explain the underlying biological mechanisms.

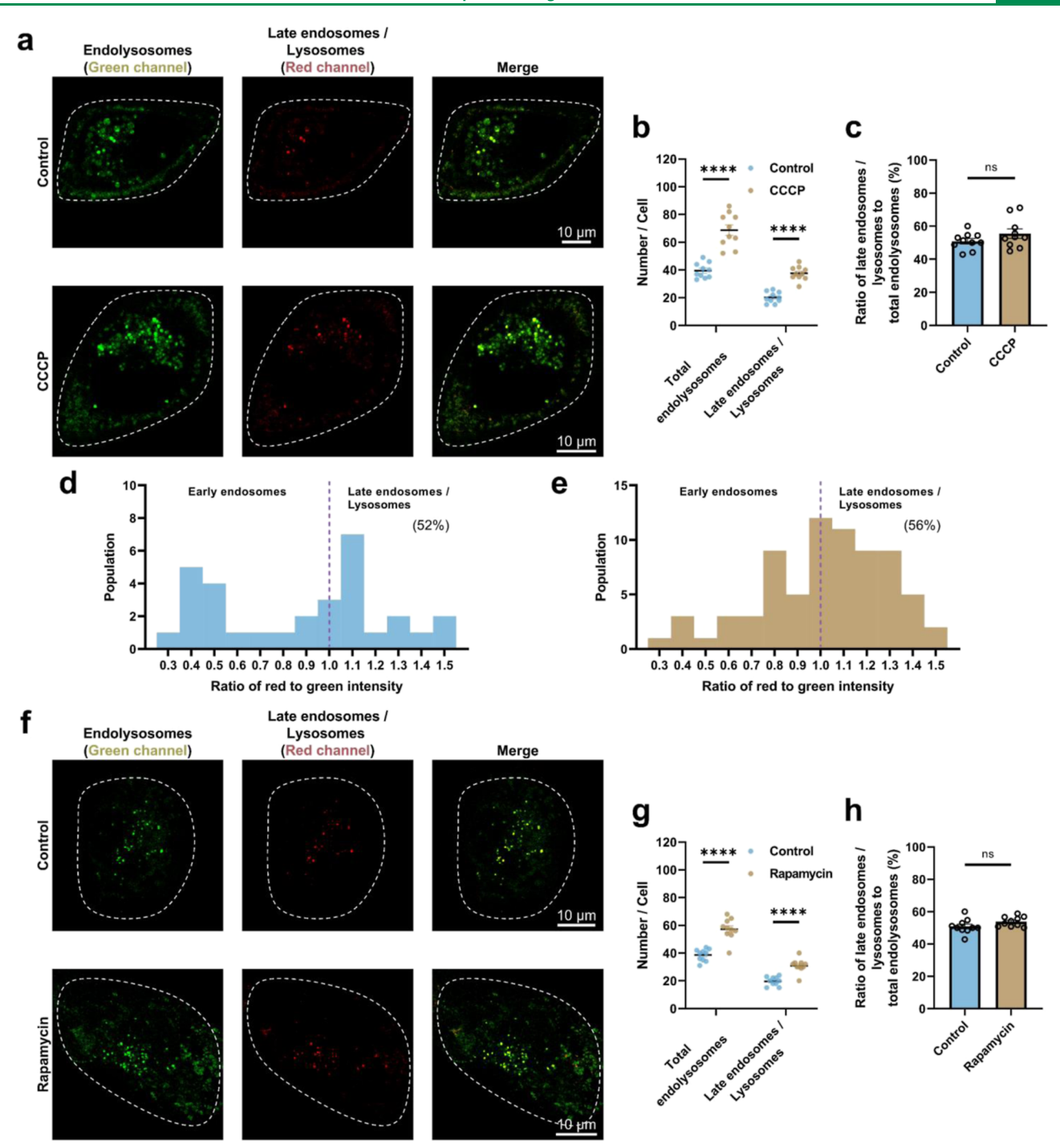


**Figure 6.** Dynamics of PyQPMe-stained endolysosomes during autophagy. (a) Confocal images of HeLa cells incubated with PyQPMe following treatment with or without CCCP for 24 h. (b) Quantification of total endolysosomes and late endosomes/lysosomes in PyQPMe-stained HeLa cells with or without CCCP treatment. (c) Ratio of the number of late endosomes/lysosomes to total endolysosomes in PyQPMe-stained HeLa cells treated with or without CCCP. (d) Quantification of ratio of red to green intensity in PyQPMe-stained HeLa cells without CCCP treatment. (e) Quantification of ratio of red to green intensity in PyQPMe-stained HeLa cells with CCCP treatment for 24 h. (f) Confocal images of HeLa cells incubated with PyQPMe following treatment with or without rapamycin for 24 h. (g) Quantification of total endolysosomes and late endosomes/lysosomes in PyQPMe-stained HeLa cells with or without rapamycin treatment. (h) Ratio of the number of late endosomes/lysosomes to total endolysosomes in PyQPMe-stained HeLa cells treated with or without rapamycin. Data are given as  $M \pm \text{SEM}$  (n = 10 independent samples from 10 cells for each statistical analysis); the statistical differences were analyzed by Student's t test, p < 0.05 is considered to be statistical significant (\*\*\*\*\* $p \le 0.0001$ ; ns p > 0.05).

Dynamics of PyQPMe-Stained Endolysosomes during Autophagy. Autophagy is a natural degradation process of cells that removes unnecessary or damaged biological macromolecules or organelles to maintain homeostasis. After

autophagosomes engulf unnecessary components, both late endosomes and lysosomes can fuse with autophagosomes to degrade autophagosomal cargo by forming amphisomes and autolysosomes, respectively.<sup>51–53</sup> To study the behavior of

endolysosomes during autophagy, carbonyl cyanide m-chlorophenyl hydrazone (CCCP), a common inducer for mitophagy (one type of autophagy), was exploited to induce autophagy in PyQPMe-stained cells.  $^{8,23}$  Cells were treated with 10  $\mu$ M CCCP for 24 h prior to PyQPMe staining. We observed a significant increase in the number of total endolysosomes and late endosomes/lysosomes in CCCP-treated HeLa cells compared with controls (Figures 6a,b and S25). However, the ratio of late endosomes/lysosomes to total endolysosomes remained stable (~55%) during the mitophagy process (Figure 6c). To further prove this phenomenon, we compared fluorescence intensity of PyQPMe-stained endolysosomes in green and red channel images. As we mentioned above (Figure 2c), pH 5-6 is the cutoff point for the red to green fluorescence intensity ratio of PyQPMe, which perfectly matches the pH changes during conversion from early endosomes to late endosomes. Hence, we briefly define that a population of early endosomes is indicated when the ratio of red to green fluorescence intensity is less than 1. Inversely, when the ratio is greater than 1, it represents the population of late endosomes/lysosomes (Figures 3d, 6d,e, and S26). As shown above, we first found that the population of both early endosomes and late endosomes were increased after CCCP treatment. Then, with quantification of the ratio of red to green intensity, we discovered that both early and late endosomes became more acidic during mitophagy, as revealed by rightward shifts among their population distributions. Furthermore, the ratio of late endosomes/lysosomes to total endolysosomes remained similar for HeLa cells treated with (56%, Figure 6e) or without (52%, Figure 6d) CCCP, which is consistent with the results in Figure 6c.

Rapamycin, a classical autophagy inducer, activates autophagy by inhibiting mTOR protein activation. 54-56 To investigate the effect of rapamycin on endolysosomes, we treated HeLa cells with 0.5  $\mu$ M rapamycin for 24 h prior to PyOPMe staining. As shown in Figure 6f, the rapamycin-treated cells showed more fluorescent spots in both green and red channels. To track the dynamics of endolysosomes in classical autophagy, we then quantified the total endolysosomes and late endosomes/ lysosomes in rapamycin-treated cells. The results showed that the number of total endolysosomes and late endosomes/ lysosomes significantly increased in rapamycin-treated HeLa cells (Figures 6g and S27). Meanwhile, similar to the CCCPinduced mitophagy (Figure 6a,c), the proportion of late endosomes/lysosomes to total endolysosomes remained the same (~54%) during the classical autophagy process (Figure 6h). Taken together, we concluded that the increased number of lysosomes during autophagy is caused by the augmentation of total endolysosomes, which is reflected in the constant conversion from early endosomes into late endosomes/ lysosomes.

## CONCLUSIONS

Herein, we report a novel fluorescent probe PyQPMe which possesses excellent pH-sensitive photophysical properties. This probe gives a low background noise for high-resolution imaging due to its large Stokes shift and strong fluorescence intensity. To date, fluorescent probes for targeting either lysosomes <sup>57</sup> or late endosomes <sup>58,59</sup> have been developed. However, there have not been proper probes available to track endolysosomes of different states simultaneously. There are shortcomings in using traditional biological protein markers for early endosomes and late endosomes/lysosomes. In order to track protein markers, additional fluorescent protein tags, such as green or red

fluorescent proteins (GFP and RFP), have to be used. Furthermore, the process of introducing fluorescent protein into protein markers is very time-consuming and potentially results in unknown interference with the biological functions of these protein markers. Here, we designed a small-molecule probe PyQPMe to enable the simultaneous monitoring of two fluorescence signals in endolysosomes at different stages of interest and minimize the interference from various microenvironments. To sum up, this pH-sensitive probe adds a new powerful tool for the field of endolysosome-related disease research and contributes to the development of potential drugs targeting dysfunctional endolysosome dynamics in humans.

On the biology side, previous studies have demonstrated that the number of lysosomes increases dramatically during the process of autophagy. The question regarding where the increased lysosomes come from during autophagy remains puzzling. The application of PyQPMe together with high-resolution imaging helps us answer this question. We here propose that the increase in the number of lysosomes during autophagy is caused by the augmentation of total endolysosomes; and the conversion rate from early endosomes into late endosomes/lysosomes remains constant. This result implies a complicated protein system governing the dynamics of endolysosomes, which requires a precise cooperation of multiple proteins.

#### **■ EXPERIMENTAL SECTION**

Materials. All commercially available reagents were purchased and used without further treatment, including 6-bromo-2-methylquinoline, pyridine-4-ylboronic acid, p-fluorobenzaldehyde, and 1-methylpiperazine. CCCP (#C2759) was purchased from Sigma. LTR DND-99 (LTR, #L7528) and LTDR (#L12492) were purchased from Invitrogen (Thermo Fisher Scientific). All fluorescent dyes were used under the manuals. Phosphate-buffered saline solution (#SH30256.01) was purchased from Hyclone (GE Healthcare Life Sciences). Dulbecco's modified Eagle's medium (DMEM, #11965092), fetal bovine serum (FBS, #26140079), and penicillin—streptomycin were purchased from Gibco (Thermo Fisher Scientific, USA).

**Characterization of PyQPMe.** The <sup>1</sup>H and <sup>13</sup>C NMR spectra were recorded on a Bruker Avance III HD Ascend 400 MHz NMR spectrometer. Chemical shifts for protons are referenced to the residual solvent peak (CDCl<sub>3</sub>, <sup>1</sup>H NMR: 7.26 ppm; D<sub>2</sub>O, <sup>1</sup>H NMR: 4.79 ppm; DMSO-*d*<sub>6</sub>, <sup>1</sup>H NMR: 2.50 ppm), while chemical shifts for carbons are referenced to the residual solvent peaks (CDCl<sub>3</sub>, <sup>13</sup>C NMR: 77.16 ppm, DMSO-*d*<sub>6</sub>; <sup>13</sup>C NMR: 39.51 ppm). The following abbreviations (or combinations thereof) were used to explain multiplicities: s = singlet, d = doublet, and m = multiplet. Matrix-assisted laser desorption ionization (MALDI) mass spectrometry was performed on a Bruker Biflex III MALDI-TOFMS instrument.

**Phosphate Buffer Solution.** A series of standard pH buffer solutions were prepared by mixing 0.2 M Na<sub>2</sub>HPO<sub>4</sub>,7H<sub>2</sub>O, 0.2 M KH<sub>2</sub>PO<sub>4</sub>, and 0.2 M H<sub>3</sub>PO<sub>4</sub> with varied volume ratios, and the pH values were measured by using a Mettler Toledo pH-meter.

**Absorption and Emission Measurements.** 3.0 mL of phosphate buffer solution and 6.44  $\mu$ L of probe stock solution (4.66 mM) were mixed well, and an appropriate portion of the solution was transferred to a quartz cell with 1 cm optical length to collect the absorption spectra on an Agilent Cary 8453 spectrophotometer. The fluorescence spectra were recorded on a HORIBA Fluorolog QM spectrofluorometer.

**Fluorescence Reversibility of PyQPMe.** The pH of a PyQPMe solution between pH 3.0 and pH 8.5 was adjusted back and forth by adding 2.0 M KOH or 3.0 M HCl, which was monitored by a Mettler Toledo pH meter.

**Computational Methods.** All calculations were performed with the Gaussian 16W program package employing the DFT method with Becke's three-parameter hybrid functional and Lee–Yang–Parr's gradient corrected correlation functional (B3LYP). 60–62 6-31G\* basis

ACS Sensors pubs.acs.org/acssensors Article

set was applied for H, C, O, and N. The geometries of the singlet ground states of compounds were optimized in  $\rm H_2O$  using the conductive polarizable continuum model (CPCM). The local minimum on each potential energy surface was confirmed by frequency analysis. Time-dependent DFT calculations produced the singlet excited states of each compound starting from the optimized geometry of the corresponding singlet ground state, using the CPCM method with  $\rm H_2O$  as the solvent. The calculated absorption spectra, electronic transition contributions, and EDDMs were generated by GaussSum 3.0.  $^{63}$  The electronic orbitals were visualized using VMD 1.9.4a51.  $^{64}$ 

Measurements of Hydrophilicity. Hydrophilicity was determined by a shake-flask ultraviolet spectrophotometry method to measure the *n*-octanol/water partition coefficients (log P). First, 25 mL of *n*-octanol and 25 mL of water were mixed at room temperature. After 24 h, the standard solutions of the sample (10  $\mu$ M) were prepared by using the preceding saturated n-octanol phase and water phase solution, respectively. Later, the test solutions were prepared by mixing 10 mL of standard solution in *n*-octanol and 10 mL of standard solution in water. After shaking, the mixture of test solution was centrifuged for 5 min. The n-octanol phase layer was separated from the water phase layer, and the absorbance of the two layers was measured by an Agilent Cary 8453 spectrophotometer. Based on the Beer-Lambert law, the concentrations of the sample in the *n*-octanol phase  $(C_0)$  and the water phase  $(C_w)$  were calculated. Finally, the *n*-octanol/water partition coefficients (log P) were further calculated by using the following equation.

$$Log P = Log(C_o/C_w)$$

**Cell Culture.** HeLa cells and PC12 cells were gifted from Dr. Carolyn M. Price lab (University of Cincinnati) and Dr. Kai Zhang lab (the University of Illinois at Urbana-Champaign), respectively. Cells were cultured in DMEM supplemented with 10% FBS (Gibco BRL), 100  $\mu$ g/mL streptomycin (Gibco BRL), and 100 U/mL penicillin (Gibco BRL). The cells were cultured at 37 °C with 5% CO<sub>2</sub> in a humidified incubator.

**Leica Stellaris 8 Confocal Imaging.** High-resolution images were acquired on a commercial Leica Stellaris 8 confocal microscope under a LIGHTNING mode. Laser powers were set at 10% intensity for 405 and 640 nm channels. The objective was  $63\times/1.4$ . High-resolution images were captured from the randomly selected field of view and analyzed with Leica LAS X and ImageJ software. All the images were exported on the Auto scale of Leica LAS X software. Cells were seeded on glassed-bottomed cell dishes (MatTek) for 24 h. Cells stained with PyQPMe (20 nM, 10 min) were treated with wortmannin (1  $\mu$ M, 24 h), CCCP (10  $\mu$ M, 24 h), rapamycin (0.5  $\mu$ M, 24 h), chloroquine (25  $\mu$ M, 30 min), and NH<sub>4</sub>Cl (50 mM, 30 min). All PCC values were analyzed in the CellProfiler.

**Cell Viability and Cytotoxicity Assay.** HeLa cells were seeded in a 96-well plate at a density of  $1\times 10^4$  cells per well in  $100~\mu L$  culture medium with different concentrations of PyQPMe at a given time. The viability was determined by adding  $10~\mu L$  of the reagent from a CCK-8 (Dojindo Molecular Technologies, Inc.) and incubating at  $37~^{\circ} C$  for 1 h. CCK-8 solution was added to each well, and the OD value for each well was read at wavelength 490 nm on a microplate reader (BioTek Instruments, Inc., USA). The interference of absorbance from PyQPMe at 490 nm was minimal compared to the CCK-8 reagent during measurement.

**Statistical Analysis.** Statistics and graphing were performed by using GraphPad Prism 9 and Excel.

# ASSOCIATED CONTENT

### **Supporting Information**

The Supporting Information is available free of charge at https://pubs.acs.org/doi/10.1021/acssensors.3c00340.

Detailed synthesis procedures and characterization of compounds, UV—vis absorption studies, fluorescence spectra, cell viability assay, bioimaging figures, data set for

statistics, calculated absorption spectra, and DFT calculations (PDF)

### AUTHOR INFORMATION

#### **Corresponding Authors**

Yujie Sun — Department of Chemistry, University of Cincinnati, Cincinnati, Ohio 45221, United States; orcid.org/0000-0002-4122-6255; Email: yujie.sun@uc.edu

Jiajie Diao – Department of Cancer Biology, College of Medicine, University of Cincinnati, Cincinnati, Ohio 45267, United States; orcid.org/0000-0003-4288-3203; Email: jiajie.diao@uc.edu

#### **Authors**

Rui Chen – Department of Chemistry, University of Cincinnati, Cincinnati, Ohio 45221, United States

Lei Wang – Department of Cancer Biology, College of Medicine, University of Cincinnati, Cincinnati, Ohio 45267, United States

Guodong Ding – Department of Chemistry, University of Cincinnati, Cincinnati, Ohio 45221, United States

Guanqun Han – Department of Chemistry, University of Cincinnati, Cincinnati, Ohio 45221, United States

Kangqiang Qiu — Department of Cancer Biology, College of Medicine, University of Cincinnati, Cincinnati, Ohio 45267, United States

Complete contact information is available at: https://pubs.acs.org/10.1021/acssensors.3c00340

#### **Author Contributions**

R.C. characterized the photophysical properties of the probe and analyzed all the imaging data. L.W. performed cell toxicity experiments. G.D. synthesized probe. G.H. performed the computational analysis. K.Q. helped process the imaging data. Y.S. and J.D. conceived the project, designed the experiments, and wrote the manuscript with the help of all authors.

#### **Notes**

The authors declare no competing financial interest.

## ■ ACKNOWLEDGMENTS

Y.S. acknowledges the support of the National Science Foundation (CHE1955358) and the University of Cincinnati. J.D. is supported by the National Institute of Health (R35GM128837).

## REFERENCES

- (1) Mizushima, N.; Komatsu, M. Autophagy: renovation of cells and tissues. *Cell* **2011**, *147*, 728–741.
- (2) Yorimitsu, T.; Klionsky, D. J. Autophagy: molecular machinery for self-eating. *Cell Death Differ.* **2005**, *12*, 1542–1552.
- (3) Klionsky, D. J.; Emr, S. D. Autophagy as a regulated pathway of cellular degradation. *Science* **2000**, 290, 1717–1721.
- (4) Xu, H.; Ren, D. Lysosomal physiology. Annu. Rev. Physiol. 2015, 77, 57-80.
- (5) De Duve, C.; Wattiaux, R. Functions of lysosomes. *Annu. Rev. Physiol.* **1966**, 28, 435–492.
- (6) Maxfield, F. R. Role of endosomes and lysosomes in human disease. Cold Spring Harbor Perspect. Biol. 2014, 6, a016931.
- (7) Nixon, R. A. Endosome function and dysfunction in Alzheimer's disease and other neurodegenerative diseases. *Neurobiol. Aging* **2005**, 26, 373–382.
- (8) Chen, Q.; Hao, M.; Wang, L.; Li, L.; Chen, Y.; Shao, X.; Tian, Z.; Pfuetzner, R. A.; Zhong, Q.; Brunger, A. T.; Guan, J.-L.; Diao, J.

- Prefused lysosomes cluster on autophagosomes regulated by VAMP8. *Cell Death Dis.* **2021**, *12*, 939.
- (9) Han, Y.; Li, M.; Qiu, F.; Zhang, M.; Zhang, Y.-H. Cell-permeable organic fluorescent probes for live-cell long-term super-resolution imaging reveal lysosome-mitochondrion interactions. *Nat. Commun.* **2017**, *8*, 1307.
- (10) Hung, Y.-H.; Chen, L. M.-W.; Yang, J.-Y.; Yuan Yang, W. Spatiotemporally controlled induction of autophagy-mediated lysosome turnover. *Nat. Commun.* **2013**, *4*, 2111.
- (11) Song, Y.; Zhang, H.; Wang, X.; Geng, X.; Sun, Y.; Liu, J.; Li, Z. One stone, three birds: pH triggered transformation of aminopyronine and iminopyronine based lysosome targeting viscosity probe for cancer visualization. *Anal. Chem.* **2021**, *93*, 1786–1791.
- (12) Wang, L.; Xiao, Y.; Tian, W.; Deng, L. Activatable rotor for quantifying lysosomal viscosity in living cells. *J. Am. Chem. Soc.* **2013**, 135, 2903–2906.
- (13) Chai, L.; Liang, T.; An, Q.; Hu, W.; Wang, Y.; Wang, B.; Su, S.; Li, C. Near-infrared in and out: observation of autophagy during stroke via a lysosome-targeting two-photon viscosity-dependent probe. *Anal. Chem.* **2022**, *94*, 5797–5804.
- (14) Jiang, J.; Tian, X.; Xu, C.; Wang, S.; Feng, Y.; Chen, M.; Yu, H.; Zhu, M.; Meng, X. A two-photon fluorescent probe for real-time monitoring of autophagy by ultrasensitive detection of the change in lysosomal polarity. *Chem. Commun.* **2017**, *53*, 3645–3648.
- (15) Li, M.; Fan, J.; Li, H.; Du, J.; Long, S.; Peng, X. A ratiometric fluorescence probe for lysosomal polarity. *Biomaterials* **2018**, *164*, 98–105.
- (16) Fan, L.; Wang, X.; Ge, J.; Li, F.; Wang, X.; Wang, J.; Shuang, S.; Dong, C. A lysosome-targeting and polarity-specific fluorescent probe for cancer diagnosis. *Chem. Commun.* **2019**, *55*, 4703–4706.
- (17) Casey, J. R.; Grinstein, S.; Orlowski, J. Sensors and regulators of intracellular pH. *Nat. Rev. Mol. Cell Biol.* **2010**, *11*, 50–61.
- (18) Yue, Y.; Huo, F.; Lee, S.; Yin, C.; Yoon, J. A review: the trend of progress about pH probes in cell application in recent years. *Analyst* **2017**, *142*, 30–41.
- (19) Lv, W.; Zhang, Z.; Zhang, K. Y.; Yang, H.; Liu, S.; Xu, A.; Guo, S.; Zhao, Q.; Huang, W. A mitochondria-targeted photosensitizer showing improved photodynamic therapy effects under hypoxia. *Angew. Chem., Int. Ed.* **2016**, *55*, 9947–9951.
- (20) Wan, Q.; Chen, S.; Shi, W.; Li, L.; Ma, H. Lysosomal pH rise during heat shock monitored by a lysosome-targeting near-infrared ratiometric fluorescent probe. *Angew. Chem., Int. Ed.* **2014**, *53*, 10916–10920.
- (21) Xu, W.; Zeng, Z.; Jiang, J.-H.; Chang, Y.-T.; Yuan, L. Discerning the chemistry in individual organelles with small-molecule fluorescent probes. *Angew. Chem., Int. Ed.* **2016**, *55*, 13658–13699.
- (22) Qiu, K.; Seino, R.; Han, G.; Ishiyama, M.; Ueno, Y.; Tian, Z.; Sun, Y.; Diao, J. De novo design of a membrane-anchored probe for multidimensional quantification of endocytic dynamics. *Adv. Health-care Mater.* **2022**, *11*, 2102185.
- (23) Wang, L.; Chen, R.; Han, G.; Liu, X.; Huang, T.; Diao, J.; Sun, Y. Super-resolution analyzing spatial organization of lysosomes with an organic fluorescent probe. *Exploration* **2022**, *2*, 20210215.
- (24) Qiu, K.; Yadav, A.; Tian, Z.; Guo, Z.; Shi, D.; Nandi, C. K.; Diao, J. Ultralong-term super-resolution tracking of lysosomes in brain organoids by near-infrared noble metal nanoclusters. *ACS Mater. Lett.* **2022**, *4*, 1565–1573.
- (25) Grossi, M.; Morgunova, M.; Cheung, S.; Scholz, D.; Conroy, E.; Terrile, M.; Panarella, A.; Simpson, J. C.; Gallagher, W. M.; O'Shea, D. F. Lysosome triggered near-infrared fluorescence imaging of cellular trafficking processes in real time. *Nat. Commun.* **2016**, *7*, 10855.
- (26) Vegesna, G. K.; Janjanam, J.; Bi, J.; Luo, F.-T.; Zhang, J.; Olds, C.; Tiwari, A.; Liu, H. pH-activatable near-infrared fluorescent probes for detection of lysosomal pH inside living cells. *J. Mater. Chem. B* **2014**, *2*, 4500–4508.
- (27) De Marco, R. J.; Thiemann, T.; Groneberg, A. H.; Herget, U.; Ryu, S. Optogenetically enhanced pituitary corticotroph cell activity post-stress onset causes rapid organizing effects on behaviour. *Nat. Commun.* **2016**, *7*, 12620.

- (28) Thomas, J. A. Optical imaging probes for biomolecules: an introductory perspective. *Chem. Soc. Rev.* **2015**, *44*, 4494–4500.
- (29) Chen, Q.; Fang, H.; Shao, X.; Tian, Z.; Geng, S.; Zhang, Y.; Fan, H.; Xiang, P.; Zhang, J.; Tian, X.; Zhang, K.; He, W.; Guo, Z.; Diao, J. A dual-labeling probe to track functional mitochondria—lysosome interactions in live cells. *Nat. Commun.* **2020**, *11*, 6290.
- (30) Fang, H.; Geng, S.; Hao, M.; Chen, Q.; Liu, M.; Liu, C.; Tian, Z.; Wang, C.; Takebe, T.; Guan, J.-L.; Chen, Y.; Guo, Z.; He, W.; Diao, J. Simultaneous Zn<sup>2+</sup> tracking in multiple organelles using superresolution morphology-correlated organelle identification in living cells. *Nat. Commun.* **2021**, *12*, 109.
- (31) Qiu, K.; Zou, W.; Fang, H.; Hao, M.; Mehta, K.; Tian, Z.; Guan, J. L.; Zhang, K.; Huang, T.; Diao, J. Light-activated mitochondrial fission through optogenetic control of mitochondria-lysosome contacts. *Nat. Commun.* **2022**, *13*, 4303.
- (32) Chen, Q.; Shao, X.; Hao, M.; Fang, H.; Guan, R.; Tian, Z.; Li, M.; Wang, C.; Ji, L.; Chao, H.; Guan, J. L.; Diao, J. Quantitative analysis of interactive behavior of mitochondria and lysosomes using structured illumination microscopy. *Biomaterials* **2020**, 250, 120059.
- (33) Fang, H.; Chen, Y.; Geng, S.; Yao, S.; Guo, Z.; He, W. Superresolution imaging of mitochondrial HClO during cell ferroptosis using a near-infrared fluorescent probe. *Anal. Chem.* **2022**, *94*, 17904–17912.
- (34) González-Domínguez, I.; Puente-Massaguer, E.; Cervera, L.; Gòdia, F. Quantification of the HIV-1 virus-like particle production process by super-resolution imaging: from VLP budding to nanoparticle analysis. *Biotechnol. Bioeng.* **2020**, *117*, 1929–1945.
- (35) Borlinghaus, R. T.; Kappel, C. HyVolution—the smart path to confocal super-resolution. *Nat. Methods* **2016**, *13*, i—iii.
- (36) Hanne, J.; Zila, V.; Heilemann, M.; Müller, B.; Kräusslich, H.-G. Super-resolved insights into human immunodeficiency virus biology. *FEBS Lett.* **2016**, *590*, 1858–1876.
- (37) Chojnacki, J.; Eggeling, C. Super-resolution fluorescence microscopy studies of human immunodeficiency virus. *Retrovirology* **2018**, *15*, 41.
- (38) Shen, W.; Wang, L.; Zhu, S.; Yu, S.; Cai, C.; Yi, W.; Zhu, Q. A dicyanoisophorone-based, near-infrared, lysosome-targeting pH sensor with an extremely large Stokes shift. *Anal. Biochem.* **2020**, 596, 113609.
- (39) Gero, A.; Markham, J. J. Studies on pyridines: I. the basicity of pyridine bases. J. Org. Chem. 1951, 16, 1835–1838.
- (40) Zhang, X.-F.; Zhang, T.; Shen, S.-L.; Miao, J.-Y.; Zhao, B.-X. A ratiometric lysosomal pH probe based on the naphthalimide—rhodamine system. *J. Mater. Chem. B* **2015**, *3*, 3260–3266.
- (41) Horobin, R. W.; Rashid-Doubell, F.; Pediani, J. D.; Milligan, G. Predicting small molecule fluorescent probe localization in living cells using QSAR modeling. 1. Overview and models for probes of structure, properties and function in single cells. *Biotech. Histochem.* **2013**, *88*, 440–460.
- (42) Qiu, K.; Chen, Y.; Rees, T. W.; Ji, L.; Chao, H. Organelle-targeting metal complexes: from molecular design to bio-applications. *Coord. Chem. Rev.* **2019**, 378, 66–86.
- (43) Qiu, K.; Liu, Y.; Huang, H.; Liu, C.; Zhu, H.; Chen, Y.; Ji, L.; Chao, H. Biscylometalated iridium(III) complexes target mitochondria or lysosomes by regulating the lipophilicity of the main ligands. *Dalton Trans.* **2016**, *45*, 16144–16147.
- (44) Qiu, K.; Huang, H.; Liu, B.; Liu, Y.; Zhang, P.; Chen, Y.; Ji, L.; Chao, H. Mitochondria-specific imaging and tracking in living cells with two-photon phosphorescent iridium(III) complexes. *J. Mater. Chem. B* **2015**, *3*, 6690–6697.
- (45) Mauthe, M.; Orhon, I.; Rocchi, C.; Zhou, X.; Luhr, M.; Hijlkema, K.-J.; Coppes, R. P.; Engedal, N.; Mari, M.; Reggiori, F. Chloroquine inhibits autophagic flux by decreasing autophagosome-lysosome fusion. *Autophagy* **2018**, *14*, 1435–1455.
- (46) Hart, P. D.; Young, M. R. Ammonium chloride, an inhibitor of phagosome-lysosome fusion in macrophages, concurrently induces phagosome-endosome fusion, and opens a novel pathway: studies of a pathogenic mycobacterium and a nonpathogenic yeast. *J. Exp. Med.* **1991**, *174*, 881–889.
- (47) Punnonen, E.-L.; Ryhänen, K.; Marjomi, V. S. At reduced temperature, endocytic membrane traffic is blocked in multivesicular

ACS Sensors pubs.acs.org/acssensors Article

carrier endosomes in rat cardiac myocytes. Eur. J. Cell Biol. 1998, 75, 344–352.

- (48) Liu, K.; Jian, Y.; Sun, X.; Yang, C.; Gao, Z.; Zhang, Z.; Liu, X.; Li, Y.; Xu, J.; Jing, Y.; Mitani, S.; He, S.; Yang, C. Negative regulation of phosphatidylinositol 3-phosphate levels in early-to-late endosome conversion. *J. Cell Biol.* **2016**, *212*, 181–198.
- (49) Shpetner, H.; Joly, M.; Hartley, D.; Corvera, S. Potential sites of PI-3 kinase function in the endocytic pathway revealed by the PI-3 kinase inhibitor, wortmannin. *J. Cell Biol.* **1996**, *132*, 595–605.
- (50) Spiro, D. J.; Boll, W.; Kirchhausen, T.; Wessling-Resnick, M. Wortmannin alters the transferrin receptor endocytic pathway in vivo and in vitro. *Mol. Biol. Cell* **1996**, *7*, 355–367.
- (51) Dingjan, I.; Linders, P. T. A.; Verboogen, D. R. J.; Revelo, N. H.; ter Beest, M.; van den Bogaart, G. Endosomal and phagosomal SNAREs. *Physiol. Rev.* **2018**, *98*, 1465–1492.
- (52) Nakatogawa, H. Mechanisms governing autophagosome biogenesis. *Nat. Rev. Mol. Cell Biol.* **2020**, 21, 439–458.
- (53) Hurley, J. H.; Schulman, B. A. Atomistic autophagy: the structures of cellular self-digestion. *Cell* **2014**, *157*, 300–311.
- (54) Xu, Y.; Yuan, J.; Lipinski, M. M. Live imaging and single-cell analysis reveal differential dynamics of autophagy and apoptosis. *Autophagy* **2013**, *9*, 1418–1430.
- (55) Vakifahmetoglu-Norberg, H.; Xia, H.-g.; Yuan, J. Pharmacologic agents targeting autophagy. *J. Clin. Invest.* **2015**, *125*, 5–13.
- (56) Chen, Q.; Shao, X.; Tian, Z.; Chen, Y.; Mondal, P.; Liu, F.; Wang, F.; Ling, P.; He, W.; Zhang, K.; Guo, Z.; Diao, J. Nanoscale monitoring of mitochondria and lysosome interactions for drug screening and discovery. *Nano Res.* **2019**, *12*, 1009–1015.
- (57) Lv, H.-S.; Huang, S.-Y.; Xu, Y.; Dai, X.; Miao, J.-Y.; Zhao, B.-X. A new fluorescent pH probe for imaging lysosomes in living cells. *Bioorganic Med. Chem. Lett.* **2014**, 24, 535–538.
- (58) Wallabregue, A.; Moreau, D.; Sherin, P.; Moneva Lorente, P.; Jarolímová, Z.; Bakker, E.; Vauthey, E.; Gruenberg, J.; Lacour, J. Selective imaging of late endosomes with a pH-sensitive diazaoxatriangulene fluorescent probe. *J. Am. Chem. Soc.* **2016**, *138*, 1752–1755.
- (59) Miao, F.; Uchinomiya, S.; Ni, Y.; Chang, Y.-T.; Wu, J. Development of pH-responsive BODIPY probes for staining late endosome in live cells. *ChemPlusChem* **2016**, *81*, 1209–1215.
- (60) Becke, A. D. Density-functional thermochemistry. I. The effect of the exchange-only gradient correction. *J. Chem. Phys.* **1992**, *96*, 2155–2160.
- (61) Becke, A. D. Density-functional exchange-energy approximation with correct asymptotic behavior. *Phys. Rev. A* **1988**, *38*, 3098–3100.
- (62) Lee, C.; Yang, W.; Parr, R. G. Development of the Colle-Salvetti correlation-energy formula into a functional of the electron density. *Phys. Rev. B* **1988**, *37*, 785–789.
- (63) O'Boyle, N. M.; Tenderholt, A. L.; Langner, K. M. Cclib: a library for package-independent computational chemistry algorithms. *J. Comput. Chem.* **2008**, 29, 839–845.
- (64) Humphrey, W.; Dalke, A.; Schulten, K. VMD: visual molecular dynamics. *J. Mol. Graphics* **1996**, *14*, 33–38.

# **□** Recommended by ACS

Fluorescence-On Imaging of Reticulophagy Enabled by an Acidity-Reporting Solvatochromic Probe

Xiaoxue Zou, Shoufa Han, et al.

JULY 18, 2023

ANALYTICAL CHEMISTRY

READ 🗹

Dual-Channel Fluorescent Probe for Detecting Viscosity and ONOO- without Signal Crosstalk in Nonalcoholic Fatty Liver

Yijia Liu, Guoqiang Feng, et al.

DECEMBER 07, 2022

ANALYTICAL CHEMISTRY

READ 🗹

Mitochondria-Targeting Multifunctional Fluorescent Probe toward Polarity, Viscosity, and ONOO and Cell Imaging

Yue Huang, Chuan Dong, et al.

JUNE 27, 2023

ANALYTICAL CHEMISTRY

READ 🗹

Super-Resolution Imaging of Mitochondrial HClO during Cell Ferroptosis Using a Near-Infrared Fluorescent Probe

Hongbao Fang, Weijiang He, et al.

DECEMBER 08, 2022

ANALYTICAL CHEMISTRY

READ **C** 

Get More Suggestions >